GEOPHYSICS, VOL. 71, NO. 6 (NOVEMBER-DECEMBER 2006); P. S209–S217, 16 FIGS.
10.1190/1.2338824

Time-shift imaging condition in seismic migration

Paul Sava[1] and Sergey Fomel[2]

ABSTRACT

Seismic imaging based on single-scattering approximation is in the analysis of the match between the source and receiver wavefields at every image location. Wavefields at depth are functions of space and time and are reconstructed from surface data either by integral methods (Kirchhoff migration) or by differential methods (reverse-time or wavefield extrapolation migration). Different methods can be used to analyze wavefield matching, of which crosscorrelation is a popular option. Implementation of a simple imaging condition requires time crosscorrelation of source and receiver wavefields, followed by extraction of the zero time lag. A generalized imaging condition operates by crosscorrelation in both space and time, followed by image extraction at zero time lag. Images at different spatial crosscorrelation lags are indicators of imaging accuracy and are also used for image-angle decomposition. In this paper, we introduce an alternative prestack imaging condition in which we preserve multiple lags of the time crosscorrelation. Prestack images are described as functions of time shifts as opposed to space shifts between source and receiver wavefields. This imaging condition is applicable to migration by Kirchhoff, wavefield extrapolation, or reverse-time techniques. The transformation allows construction of common-image gathers presented as functions of either time shift or reflection angle at every location in space. Inaccurate migration velocity is revealed by angle-domain common-image gathers with nonflat events. Computational experiments using a synthetic data set from a complex salt model demonstrate the main features of the method.

INTRODUCTION

A key challenge for imaging in complex areas is accurate determination of a velocity model in the area under investigation. Migration-velocity analysis is based on the principle that image-accuracy indicators are optimized when data are correctly imaged. A common procedure for velocity analysis is to examine the alignment of images created with multioffset data. An optimal choice of image analysis can be done in the angle domain, which is free of some complicated artifacts present in surface offset gathers in complex areas (Stolk and Symes, 2004).

Migration-velocity analysis after migration by wavefield extrapolation requires image decomposition in scattering angles relative to reflector normals. Several methods have been proposed for such decompositions (de Bruin et al., 1990; Prucha et al., 1999; Mosher and Foster, 2000; Rickett and Sava, 2002; Xie and Wu, 2002; Sava and Fomel, 2003; Soubaras, 2003; Biondi and Symes, 2004; Fomel, 2004). These procedures require decomposition of extrapolated wavefields in variables that are related to the reflection angle.

A key component of such image decompositions is the imaging condition. A careful implementation of the imaging condition preserves all information necessary to decompose images in their angle-dependent components. The challenge is efficient and reliable construction of these angle-dependent images for velocity or amplitude analysis.

In migration with wavefield extrapolation, a prestack imaging condition based on spatial shifts of the source and receiver wavefields allows for angle composition (Rickett and Sava, 2002; Sava and Fomel, 2005). Such formed angle gathers describe reflectivity as a function of reflection angles and are powerful tools for migration-velocity analysis or amplitude-versus-angle analysis. However, because of the large expense of space-time crosscorrelations, especially in three dimensions, this imaging methodology is not used routinely in data processing.

This paper presents a different form of imaging condition. The key idea of this new method is to use time shifts instead of space shifts between wavefields computed from sources and receivers. As for the space-shift imaging condition, an image is built by space-time crosscorrelations of subsurface wavefields, and multiple lags of the time crosscorrelation are preserved in the image. Time shifts have physical meaning that can be related directly to reflection geometry, similar to the procedure used for space shifts. Furthermore,

Manuscript received by the Editor September 29, 2005; revised manuscript received February 23, 2006; published online September 21, 2006.
[1]Colorado School of Mines, Department of Geophysics, 1500 Illinois Street, Golden, Colorado 80401. E-mail: psava@mines.edu.
[2]University of Texas - Austin, Bureau of Economic Geology, Austin, Texas 78758. E-mail: sergey.fomel@beg.utexas.edu.
© 2006 Society of Exploration Geophysicists. All rights reserved.

time-shift imaging is cheaper to apply than space-shift imaging, and thus it might alleviate some of the difficulties posed by costly cross-correlations in 3D space-shift imaging condition.

The idea of a time-shift imaging condition is related to the idea of depth-focusing analysis (Faye and Jeannot, 1986; MacKay and Abma, 1992, 1993; Nemeth, 1995, 1996). The main novelty of our approach is that we employ time shifting to construct angle-domain gathers for prestack depth imaging.

The time-shift imaging concept is applicable to Kirchhoff migration, migration by wavefield extrapolation, or reverse-time migration. We present a theoretical analysis of this new imaging condition, followed by a physical interpretation leading to angle decomposition. Finally, we illustrate the method with images of the complex Sigsbee 2A data set (Paffenholz et al., 2002).

IMAGING CONDITION IN WAVE-EQUATION IMAGING

A traditional imaging condition for shot-record migration, often referred to as UD^* imaging condition (Claerbout, 1985), consists of time crosscorrelation at every image location between the source and receiver wavefields, followed by image extraction at zero time:

$$U(\mathbf{m},t) = U_r(\mathbf{m},t) * U_s(\mathbf{m},t), \tag{1}$$

$$R(\mathbf{m}) = U(\mathbf{m},t=0), \tag{2}$$

where the symbol $*$ denotes crosscorrelation in time. Here, $\mathbf{m} = [m_x,m_y,m_z]$ is a vector describing the locations of image points. $U_s(\mathbf{m},t)$ and $U_r(\mathbf{m},t)$ are source and receiver wavefields, respectively; and $R(\mathbf{m})$ denotes a migrated image. A final image is obtained by summation over shots.

Space-shift imaging condition

A generalized prestack imaging condition (Sava and Fomel, 2005) estimates image reflectivity using crosscorrelation in space and time, followed by image extraction at zero time:

$$U(\mathbf{m},\mathbf{h},t) = U_r(\mathbf{m}+\mathbf{h},t) * U_s(\mathbf{m}-\mathbf{h},t), \tag{3}$$

$$R(\mathbf{m},\mathbf{h}) = U(\mathbf{m},\mathbf{h},t=0). \tag{4}$$

Here, $\mathbf{h} = [h_x,h_y,h_z]$ is a vector describing the space shift between the source and receiver wavefields prior to imaging. Special cases of this imaging condition are horizontal space shift (Rickett and Sava, 2002) and vertical space shift (Biondi and Symes, 2004).

For computational reasons, this imaging condition is usually implemented in the Fourier domain using the expression

$$R(\mathbf{m},\mathbf{h}) = \sum_{\omega} U_r(\mathbf{m}+\mathbf{h},\omega)U_s^*(\mathbf{m}-\mathbf{h},\omega). \tag{5}$$

The $*$ sign represents a complex conjugate applied on the receiver wavefield U_s in the Fourier domain.

Time-shift imaging condition

Another possible imaging condition, advocated in this paper, involves shifting the source and receiver wavefields in time, as opposed to space, followed by image extraction at zero time:

$$U(\mathbf{m},t,\boldsymbol{\tau}) = U_r(\mathbf{m},t+\boldsymbol{\tau}) * U_s(\mathbf{m},t-\boldsymbol{\tau}), \tag{6}$$

$$R(\mathbf{m},\boldsymbol{\tau}) = U(\mathbf{m},\boldsymbol{\tau},t=0). \tag{7}$$

Here, $\boldsymbol{\tau}$ is a scalar describing the time shift between the source and receiver wavefields prior to imaging. This imaging condition can be implemented in the Fourier domain using the expression

$$R(\mathbf{m},\boldsymbol{\tau}) = \sum_{\omega} U_r(\mathbf{m},\omega)U_s^*(\mathbf{m},\omega)e^{2i\omega\boldsymbol{\tau}}, \tag{8}$$

which involves a phase shift applied to the wavefields prior to summation over frequency ω for imaging at zero time.

Space-shift and time-shift imaging condition

To be even more general, we can formulate an imaging condition involving both space shift and time shift, followed by image extraction at zero time:

$$U(\mathbf{m},\mathbf{h},t) = U_r(\mathbf{m}+\mathbf{h},t+\boldsymbol{\tau}) \star U_s(\mathbf{m}-\mathbf{h},t-\boldsymbol{\tau}), \tag{9}$$

$$R(\mathbf{m},\mathbf{h},\boldsymbol{\tau}) = U(\mathbf{m},\mathbf{h},\boldsymbol{\tau},t=0). \tag{10}$$

However, the cost involved in this transformation is large, so this general form does not have immediate practical value. Imaging conditions described by equations 3 and 4 and equations 6 and 7 are special cases of equations 9 and 10 for $\mathbf{h} = 0$ and $\boldsymbol{\tau} = 0$, respectively.

ANGLE TRANSFORMATION IN WAVE-EQUATION IMAGING

Using the definitions introduced in the preceding section, we can make the standard notations for source and receiver coordinates: $\mathbf{s} = \mathbf{m} - \mathbf{h}$ and $\mathbf{r} = \mathbf{m} + \mathbf{h}$. The traveltime from a source to a receiver is a function of all spatial coordinates of the seismic experiment $t = t(\mathbf{m},\mathbf{h})$. Differentiating t with respect to all components of the vectors $\mathbf{m}$ and $\mathbf{h}$, and using the standard notations $\mathbf{p}_\alpha = \nabla_\alpha t$, where $\alpha = \{\mathbf{m},\mathbf{h},\mathbf{s},\mathbf{r}\}$, we can write

$$\mathbf{p_m} = \mathbf{p_r} + \mathbf{p_s}, \tag{11}$$

$$\mathbf{p_h} = \mathbf{p_r} - \mathbf{p_s}. \tag{12}$$

From equations 11 and 12, we can write

$$2\mathbf{p_s} = \mathbf{p_m} - \mathbf{p_h}, \tag{13}$$

$$2\mathbf{p_r} = \mathbf{p_m} + \mathbf{p_h}. \tag{14}$$

By analyzing the geometric relations of various vectors at an image point (Figure 1), we can write the following trigonometric expressions:

$$|\mathbf{p_h}|^2 = |\mathbf{p_s}|^2 + |\mathbf{p_r}|^2 - 2|\mathbf{p_s}||\mathbf{p_r}|\cos(2\theta), \tag{15}$$

$$|\mathbf{p_m}|^2 = |\mathbf{p_s}|^2 + |\mathbf{p_r}|^2 + 2|\mathbf{p_s}||\mathbf{p_r}|\cos(2\theta). \tag{16}$$

Equations 15 and 16 relate wavefield quantities $\mathbf{p_h}$ and $\mathbf{p_m}$ to a geometric quantity, reflection angle θ. Analysis of these expressions provides sufficient information for complete decompositions of migrated images in components for different reflection angles.

Space-shift imaging condition

Defining $\mathbf{k_m}$ and $\mathbf{k_h}$ as location and offset wavenumber vectors and assuming $|\mathbf{p_s}| = |\mathbf{p_r}| = s$, where $s(\mathbf{m})$ is the slowness at image locations, we can replace $|\mathbf{p_m}| = |\mathbf{k_m}|/\omega$ and $|\mathbf{p_h}| = |\mathbf{k_h}|/\omega$ in equations 15 and 16:

$$|\mathbf{k_h}|^2 = 2(\omega s)^2(1 - \cos 2\theta), \tag{17}$$

$$|\mathbf{k_m}|^2 = 2(\omega s)^2(1 + \cos 2\theta). \tag{18}$$

Using the trigonometric identity

$$\cos(2\theta) = \frac{1 - \tan^2\theta}{1 + \tan^2\theta}, \tag{19}$$

we can eliminate from equations 17 and 18 the dependence on frequency and slowness and obtain an angle decomposition formulation after imaging by expressing $\tan\theta$ as a function of position and offset wavenumbers $(\mathbf{k_m}, \mathbf{k_h})$:

$$\tan\theta = \frac{|\mathbf{k_h}|}{|\mathbf{k_m}|}. \tag{20}$$

We can construct angle-domain common-image gathers by transforming prestack migrated images using equation 20:

$$R(\mathbf{m}, \mathbf{h}) \Rightarrow R(\mathbf{m}, \theta). \tag{21}$$

In two dimensions, this transformation is equivalent with a slant stack on migrated offset gathers. For 3D, this transformation is described in more detail by Fomel (2004) or Sava and Fomel (2005).

Time-shift imaging condition

Using the same definitions as those introduced in the preceding subsection, we can rewrite equation 18 as

$$|\mathbf{p_m}|^2 = 4s^2\cos^2\theta, \tag{22}$$

from which we can derive an expression for angle transformation after time-shift prestack imaging:

$$\cos\theta = \frac{|\mathbf{p_m}|}{2s}. \tag{23}$$

Relation 23 can be interpreted using ray-parameter vectors at image locations (Figure 2). Angle-domain common-image gathers can be obtained by transforming prestack-migrated images using equation 23:

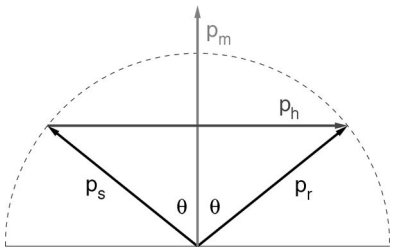


Figure 1. Geometric relations between ray vectors at a reflection point.

$$R(\mathbf{m}, \boldsymbol{\tau}) \Rightarrow R(\mathbf{m}, \theta). \tag{24}$$

Equation 23 can be written as

$$\cos^2\theta = \frac{|\nabla_{\mathbf{m}} 2\boldsymbol{\tau}|^2}{4s^2(\mathbf{m})} = \frac{\boldsymbol{\tau}_x^2 + \boldsymbol{\tau}_y^2 + \boldsymbol{\tau}_z^2}{s^2(x,y,z)}, \tag{25}$$

where $\boldsymbol{\tau}_x, \boldsymbol{\tau}_y, \boldsymbol{\tau}_z$ are partial derivatives of $\boldsymbol{\tau}$ relative to x, y, z. We can rewrite equation 25 as

$$\cos^2\theta = \frac{\boldsymbol{\tau}_z^2}{s^2(x,y,z)}(1 + z_x^2 + z_y^2), \tag{26}$$

where z_x and z_y denote the partial derivative of coordinate z relative to coordinates x and y, respectively. Equation 26 describes an algorithm in two steps for angle decomposition after time-shift imaging: Compute $\cos\theta$ through a slant stack in $z - \boldsymbol{\tau}$ panels (find a change in $\boldsymbol{\tau}$ with respect to z); then apply a correction using the migration slowness s and a function of the structural dips $\sqrt{1 + z_x^2 + z_y^2}$.

MOVEOUT ANALYSIS

We can use the Kirchhoff formulation to analyze the moveout behavior of the time-shift imaging condition in the simplest case of a flat reflector in a constant-velocity medium (Figures 3–5).

The synthetic data are imaged using shot-record wavefield extrapolation migration. Figure 4 shows offset common-image gathers for three different migration slownesses s, one of which is equal to the modeling slowness s_0. Figure 4a corresponds to the space-shift imaging condition and Figure 4b to the time-shift imaging condition.

For the space-shift common-image gathers constructed with correct slowness (Figure 4a), the energy is focused at zero offset, but it spreads in a region of offsets when the slowness is wrong. Slant stacking produces the images in Figure 5a.

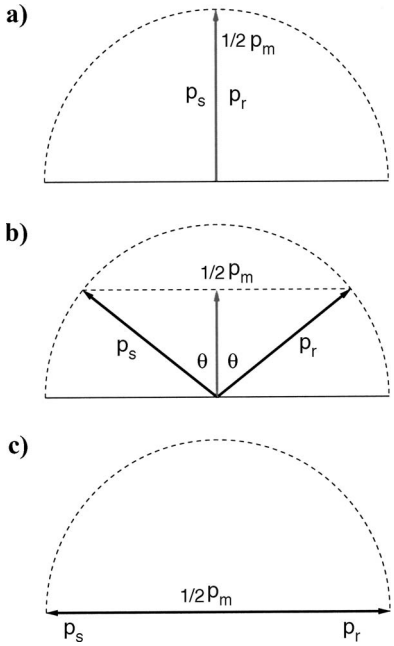


Figure 2. Interpretation of angle decomposition based on equation 23 for time-shift gathers.

For the time-shift common-image gathers constructed with correct slowness (Figure 4b), the energy is distributed along a line with a slope equal to the local velocity at the reflector position, but it spreads around this region when the slowness is wrong. Slant stacking produces the images in Figure 5b.

Let s_0 and z_0 represent the true slowness and reflector depth, and s and z stand for the corresponding quantities used in migration. An image is formed when the Kirchoff stacking curve $t(\hat{h}) = 2s\sqrt{z^2 + \hat{h}^2} + 2\boldsymbol{\tau}$ touches the true reflection response $t_0(\hat{h}) = 2s_0\sqrt{z_0^2 + \hat{h}^2}$ (Figure 3). Solving for $\hat{h}$ from the envelope condition $t'(\hat{h}) = t_0'(\hat{h})$ yields two solutions:

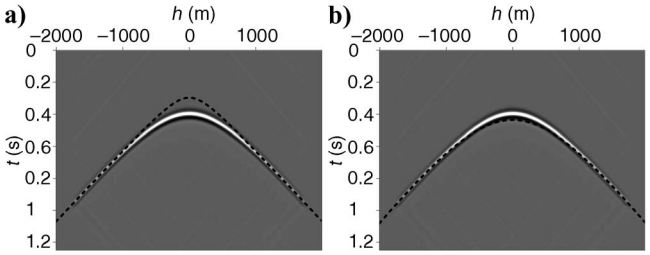


Figure 3. An image is formed when the Kirchoff stacking curve (dashed line) touches the true reflection response. (a) The case of undermigration. (b) Overmigration.

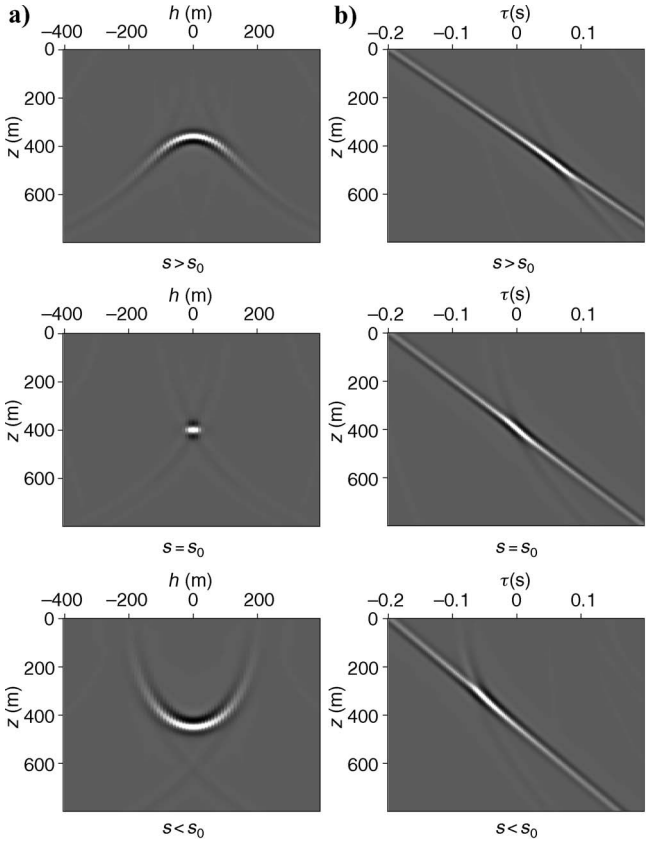


Figure 4. Common-image gathers for (a) space-shift imaging and (b) time-shift imaging.

$$\hat{h} = 0 \tag{27}$$

and

$$\hat{h} = \sqrt{\frac{s_0^2 z^2 - s^2 z_0^2}{s^2 - s_0^2}}. \tag{28}$$

Substituting solutions 27 and 28 in the condition $t(\hat{h}) = t_0(\hat{h})$ produces two images in the $\{z, \boldsymbol{\tau}\}$ space. The first image is a straight line,

$$z(\boldsymbol{\tau}) = \frac{z_0 s_0 - \boldsymbol{\tau}}{s}, \tag{29}$$

and the second image is a segment of the second-order curve,

$$z(\boldsymbol{\tau}) = \sqrt{z_0^2 + \frac{\boldsymbol{\tau}^2}{s^2 - s_0^2}}. \tag{30}$$

Applying a slant-stack transformation with $z = z_1 - \nu\boldsymbol{\tau}$ turns line 29 into a point $\{z_0 s_0/s, 1/s\}$ in $\{z_1, \nu\}$ space, while curve 30 turns into the curve

$$z_1(\nu) = z_0\sqrt{1 + \nu^2(s_0^2 - s^2)}. \tag{31}$$

The curvature of the $z_1(\nu)$ curve at $\nu = 0$ is a clear indicator of the migration-velocity errors.

By contrast, the moveout shape $z(h)$ appearing in wave-equation migration with the lateral-shift imaging condition is

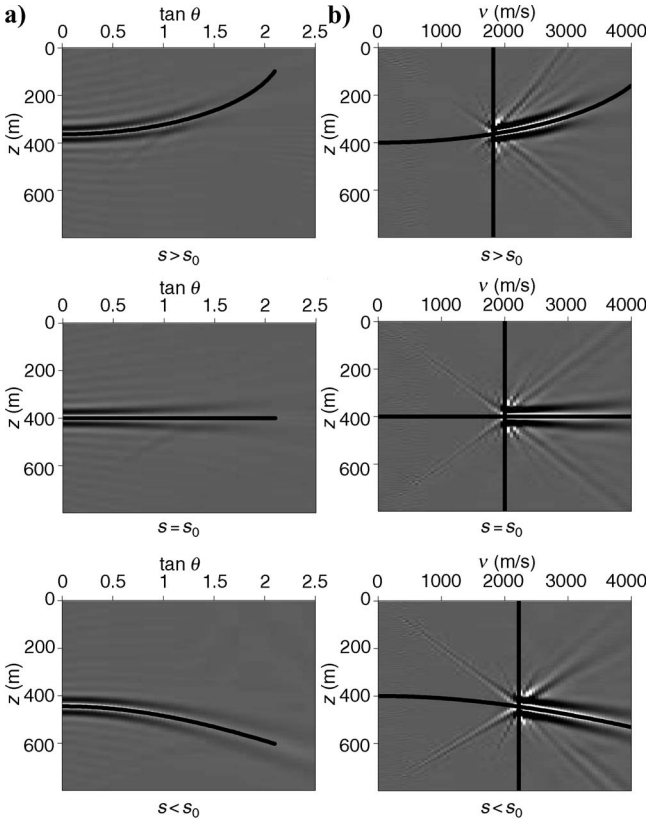


Figure 5. Common-image gathers after slant stack for (a) space-shift imaging and (b) time-shift imaging. The vertical line indicates the migration velocity.

$$z(h) = s_0\sqrt{\frac{z_0^2}{s^2} + \frac{h^2}{s^2 - s_0^2}}. \quad (32)$$

After the slant transformation $z = z_1 + h\tan\theta$, the moveout curve 32 turns into the curve

$$z_1(\theta) = \frac{z_0}{s}\sqrt{s_0^2 + \tan^2\theta(s_0^2 - s^2)}, \quad (33)$$

which is applicable for velocity analysis. A formal connection between ν-parameterization in equation 31 and θ-parameterization in equation 33 is given by

$$\tan^2\theta = s^2\nu^2 - 1 \quad (34)$$

or

$$\cos\theta = \frac{1}{\nu s} = \frac{\boldsymbol{\tau}_z}{s}, \quad (35)$$

where $\boldsymbol{\tau}_z = (\partial\boldsymbol{\tau}/\partial z)$. Equation 35 is a special case of equation 23 for flat reflectors. Curves of shapes 31 and 33 are plotted on top of the experimental moveouts in Figure 5.

TIME-SHIFT IMAGING IN KIRCHHOFF MIGRATION

The imaging condition described in the preceding section has an equivalent formulation in Kirchhoff imaging. Traditional construction of common-image gathers using Kirchhoff migration is represented by the expression

$$R(\mathbf{m},\hat{\mathbf{h}}) = \sum_{\hat{\mathbf{m}}} \hat{U}[\hat{\mathbf{m}},\hat{\mathbf{h}},t_s(\mathbf{m},\hat{\mathbf{m}} - \hat{\mathbf{h}}) + t_r(\mathbf{m},\hat{\mathbf{m}} + \hat{\mathbf{h}})], \quad (36)$$

where $\hat{U}(\hat{\mathbf{m}},\hat{\mathbf{h}},t)$ is the recorded wavefield at the surface as a function of surface midpoint $\hat{\mathbf{m}}$ and offset $\hat{\mathbf{h}}$ (Figure 6). Terms t_s and t_r stand for traveltimes from sources and receivers at coordinates $\hat{\mathbf{m}} - \hat{\mathbf{h}}$ and $\hat{\mathbf{m}} + \hat{\mathbf{h}}$ to points in the subsurface at coordinates $\mathbf{m}$. For simplicity, the amplitude- and phase-correction term $A(\mathbf{m},\hat{\mathbf{m}},\hat{\mathbf{h}})\,\partial/\partial t$ is omitted in equation 36. The time-shift imaging condition can be implemented in Kirchhoff imaging using a modification of equation 36 that is equivalent to equations 6 and 8:

$$R(\mathbf{m},\boldsymbol{\tau}) = \sum_{\hat{\mathbf{m}}}\sum_{\hat{\mathbf{h}}} \hat{U}[\hat{\mathbf{m}},\hat{\mathbf{h}},t_s(\mathbf{m},\hat{\mathbf{m}} - \hat{\mathbf{h}}) + t_r(\mathbf{m},\hat{\mathbf{m}} + \hat{\mathbf{h}}) + 2\boldsymbol{\tau}]. \quad (37)$$

Images obtained by Kirchhoff migration as discussed in equation 37 differ from images constructed with equation 36. Relation 37 involves a double summation over surface midpoint $\hat{\mathbf{m}}$ and offset $\hat{\mathbf{h}}$ to produce an image at location $\mathbf{m}$. Therefore, the entire input data contributes potentially to every image location. This is advantageous because migrating using relation 36 different offsets $\hat{\mathbf{h}}$ independently may lead to imaging artifacts as discussed by Stolk and Symes (2004). After Kirchhoff migration using relation 37, images can be converted to the angle domain using equation 23.

EXAMPLES

We demonstrate the imaging condition introduced in this paper with the Sigsbee 2A synthetic model (Paffenholz et al., 2002). Figure 7 shows the correct migration velocity and the image created by shot-record migration with wavefield extrapolation using the time-shift imaging condition. The image in Figure 7a is extracted at $\boldsymbol{\tau} = 0$.

Figure 8a shows common-image gathers at locations $x = \{7,9,11,13,15,17\}$ km obtained by time-shift imaging conditions. As in the preceding synthetic example, we can observe events with linear trends at slopes corresponding to local migration velocity. Since the migration velocity is correct, the strongest events in common-image gathers correspond to $\boldsymbol{\tau} = 0$. For comparison, Figure 8b shows common-image gathers at the same locations obtained by space-shift imaging condition. In the latter case, the strongest events

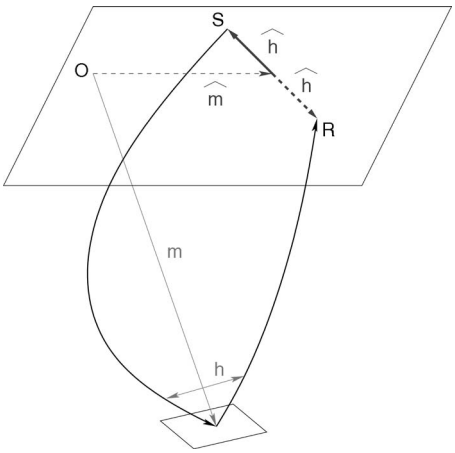


Figure 6. Notations for Kirchhoff imaging. S is a source and R is a receiver.

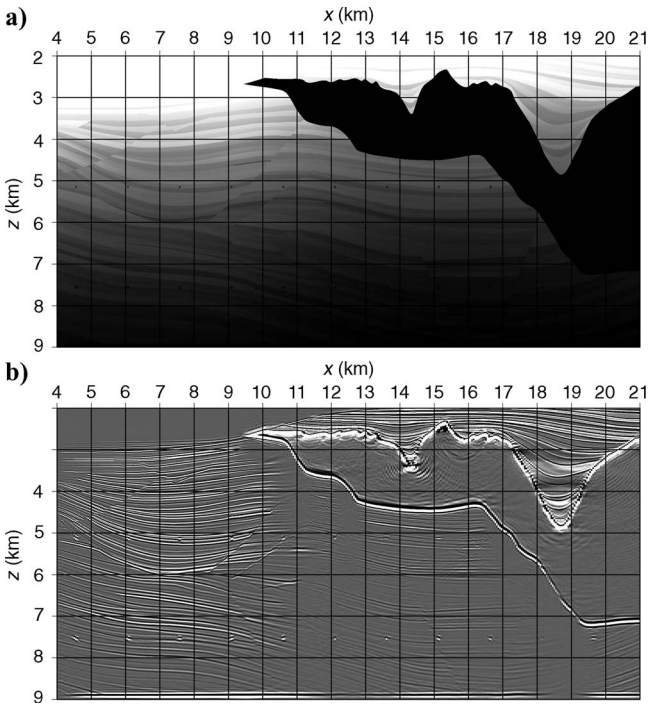


Figure 7. Sigsbee 2A model. (a) Correct velocity and (b) migrated image obtained by shot-record wavefield extrapolation migration with time-shift imaging condition.

occur at $\mathbf{h} = 0$. The zero-offset images ($\boldsymbol{\tau} = 0$ and $\mathbf{h} = 0$) are identical.

Figure 9 shows the angle decomposition for the common-image gather at location $x = 7$ km. From left to right, the panels depict the migrated image, a common-image gather resulting from migration by wavefield extrapolation with time-shift imaging, the common-image gather after slant stacking in the z–$\boldsymbol{\tau}$ plane, and an angle gather derived from the slant-stacked panel using equation 23.

For comparison, Figure 10 depicts a similar process for a common-image gather at the same location obtained by space-shift imaging. Despite the fact that the offset-gathers are completely different, the angle gathers are comparable, showing similar trends of angle-dependent reflectivity.

Figure 11a shows angle-domain common-image gathers for time-shift imaging at locations $x = \{7,9,11,13,15,17\}$ km. Since the migration velocity is correct, all events are mostly flat, indicating correct imaging. For comparison, Figure 11b shows angle-domain common-image gathers for space-shift imaging condition at the same locations in the image.

Finally, we illustrate the behavior of time-shift imaging with incorrect velocity. Figure 12a shows an incorrect velocity model used to image the Sigsbee 2A data, and Figure 12b shows the resulting image. The incorrect velocity is a smooth version of the correct interval velocity, scaled by 10% from a depth $z = 5$ km downward. The uncollapsed diffractors at depth $z = 7$ km clearly indicate velocity inaccuracy.

Figures 13 and 14 show image gathers and the derived angle gathers for time-shift and space-shift imaging at the same location, $x = 7$ km. Because of incorrect velocity, focusing does not occur at $\boldsymbol{\tau} = 0$ or $\mathbf{h} = 0$ as in the preceding case. Likewise, the reflections in angle gathers are nonflat, indicating velocity inaccuracies. Compare Figures 9 and 13 and Figures 10 and 14. Those moveouts can be exploited for migration-velocity analysis (Biondi and Sava, 1999; Clapp et al., 2004; Sava and Biondi, 2004a, b).

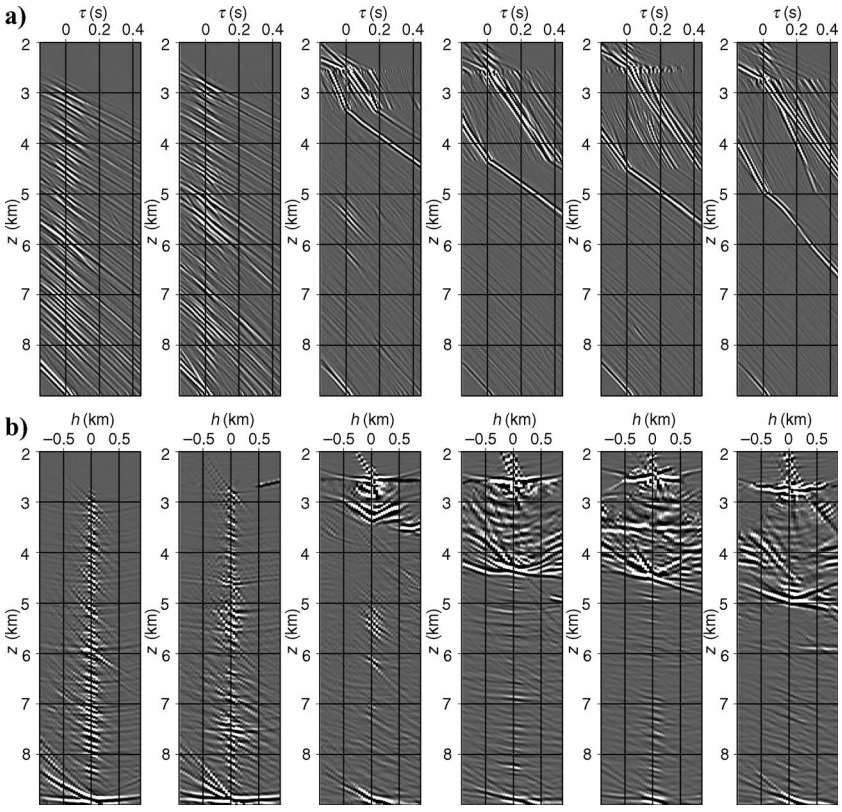


Figure 8. Imaging-gathers at positions $x = \{7,9,11,13,15,17\}$ km. (a) Time-shift imaging condition and (b) space-shift imaging condition.

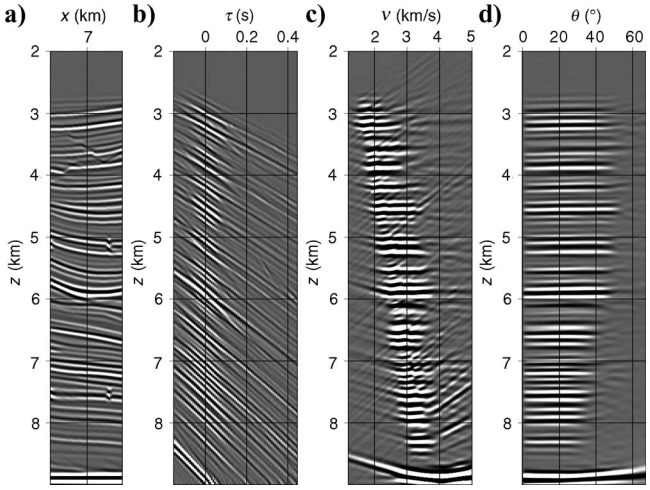


Figure 9. Time-shift imaging condition gather at $x = 7$ km. The panels depict (a) the image, (b) the time-shift gather, (c) the slant-stacked time-shift gather, and (d) the angle gather.

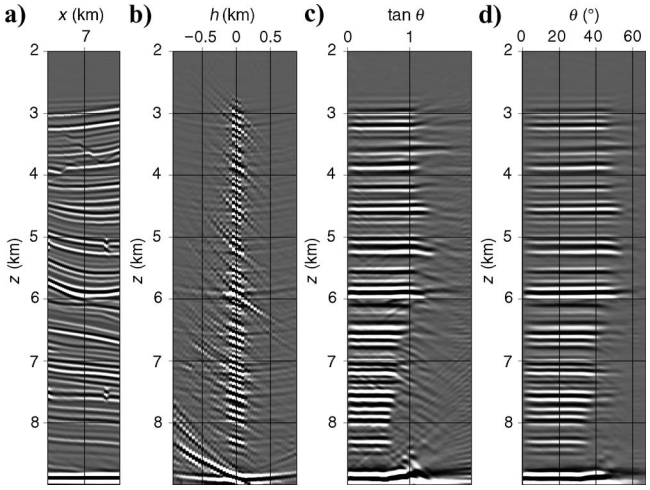


Figure 10. Space-shift imaging condition gather at $x = 7$ km. The panels depict (a) the image, (b) the space-shift gather, (c) the slant-stacked space-shift gather, and (d) the angle gather.

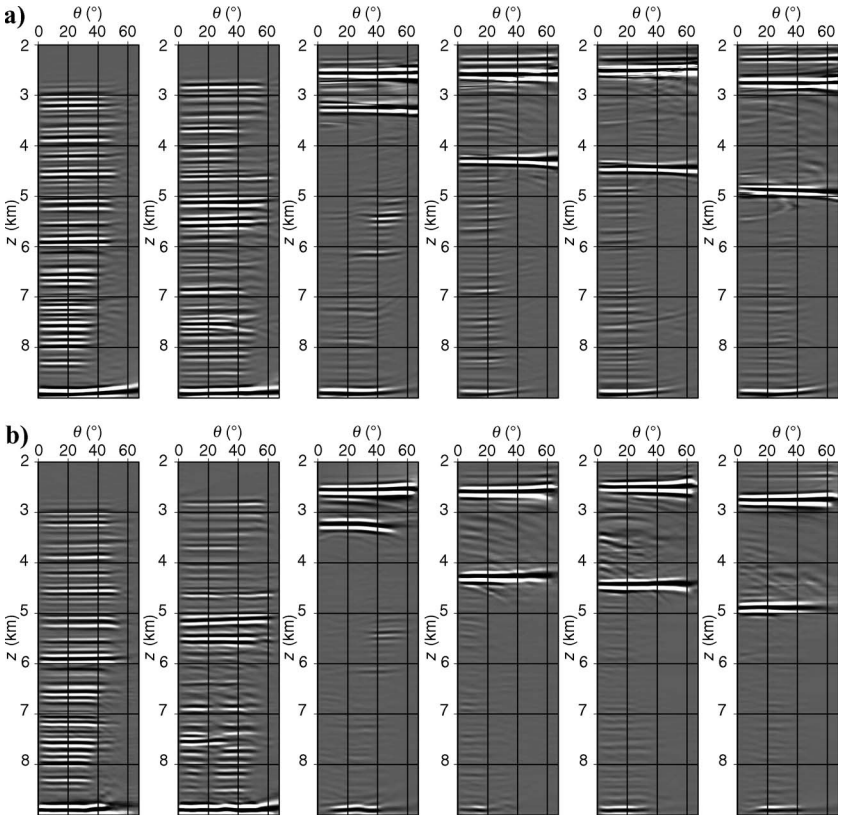


Figure 11. Angle gathers at positions $x = \{7,9,11,13,15,17\}$ km. (a) Time-shift imaging condition. (b) Space-shift imaging condition. Compare with Figure 8.

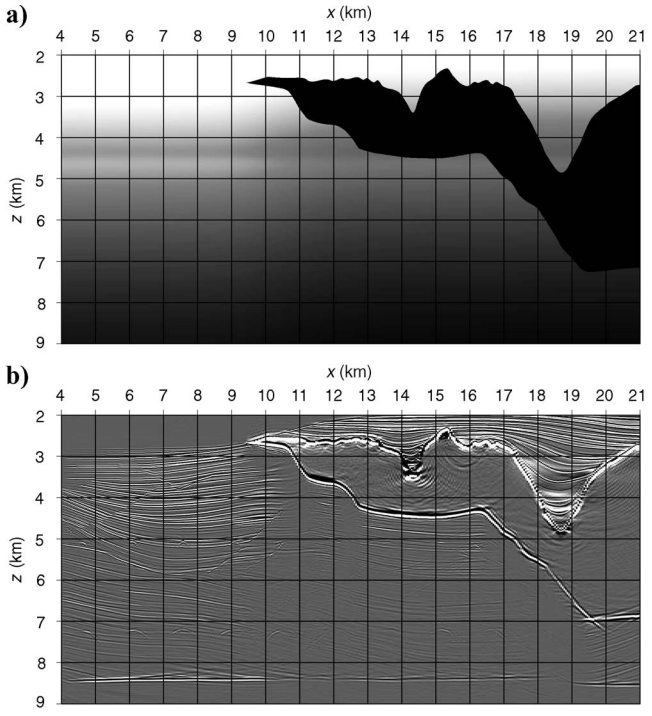


Figure 12. Sigsbee 2A model imaging shows (a) incorrect velocity and (b) migrated image obtained by shot-record wavefield extrapolation migration with time-shift imaging condition. Compare with Figure 7.

DISCUSSION

As discussed in a preceding section, time-shift gathers consist of linear events with slopes corresponding to the local migration velocity. In contrast, space-shift gathers consist of events focused at $\mathbf{h} = 0$. Those events can be mapped to the angle domain using transformations 20 and 23, respectively.

To understand the angle-domain mapping, we consider a simple synthetic in which we model common-image gathers corresponding to incidence at a particular angle. The experiment is depicted in Figure 15 for time shift imaging and in Figure 16 for space-shift imaging. For this experiment, the sampling parameters are $\Delta z = 0.01$ km, $\Delta h = 0.02$ km, and $\Delta \boldsymbol{\tau} = 0.01$ s.

A reflection event at a single angle of incidence maps in common-image gathers as a line of a given slope. The left panels in Figures 15 and 16 show three cases corresponding to angles of 0°, 20°, and 40°. Since we want to analyze how such events map to angle, we subsample each line to five selected samples lining up at the correct slope.

The middle panels in Figures 15 and 16 show the data in the left panels after slant stacking in z–$\boldsymbol{\tau}$ or z–h panels, respectively. Each individual sample from the common-image gathers maps in a line of a different slope intersecting in a point. For example, normal incidence in a time-shift gather maps at the migration velocity $v = 2$ km/s (Figure 15, top row, middle panel), and normal incidence in a space-shift gather maps at slant-stack parameter $\tan\theta = 0$.

Figures 15f and 16f show the data from the middle panels after mapping to angle using equations 23 and 20, respectively. All lines from the slant-stack panels map into curves that intersect at the angle of incidence.

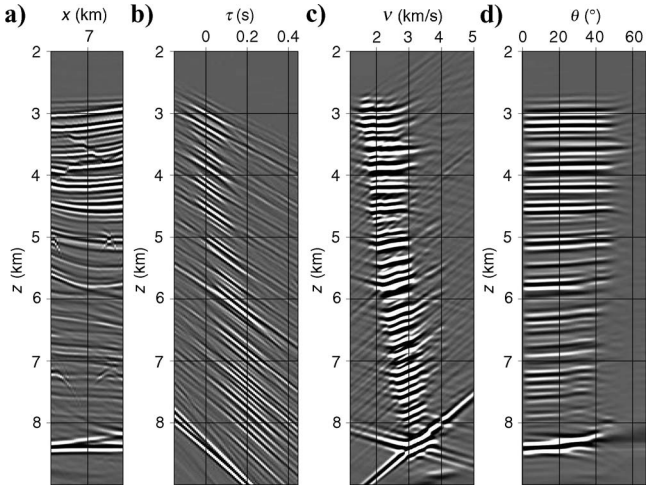


Figure 13. Time-shift imaging condition gather at $x = 7$ km. The panels depict (a) the image, (b) the offset gather, (c) the slant-stacked gather, and (d) the angle gather. Compare with Figure 9.

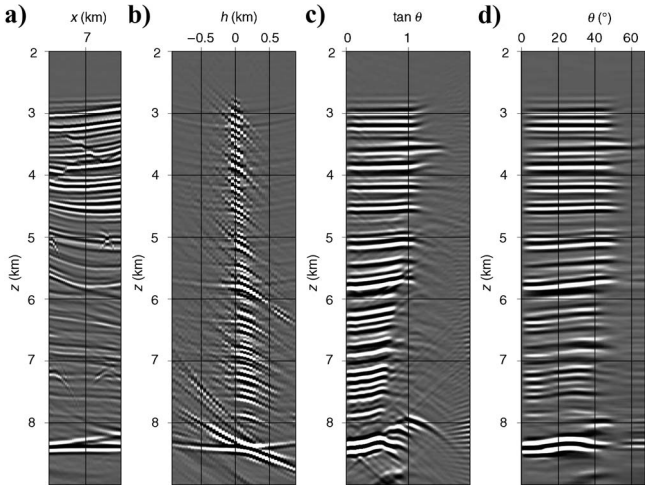


Figure 14. Space-shift imaging condition gather at $x = 7$ km. The panels depict (a) the image, (b) the offset gather, (c) the slant-stack gather, and (d) the angle gather. Compare with Figure 10.

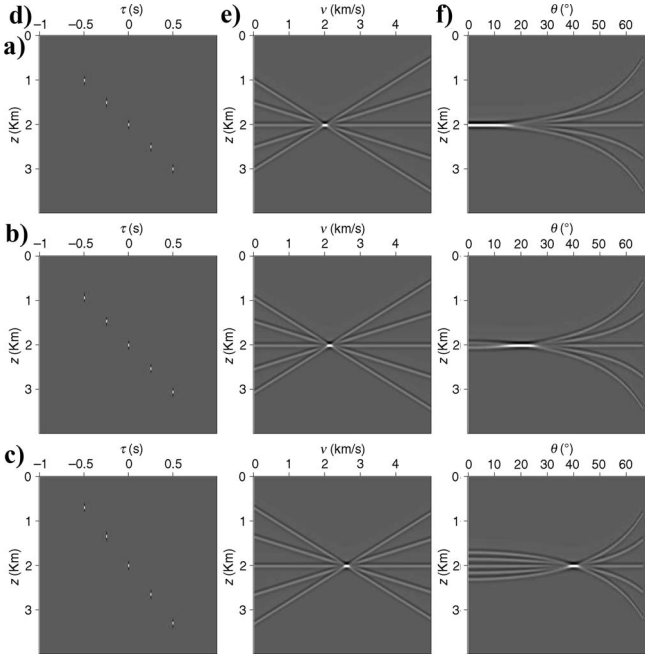


Figure 15. Image-gather formation using time-shift imaging. Horizontal rows depict events at (a) 0°, (b) 20°, and (c) 40°. Vertical columns correspond to subsampled (d) time-shift gathers, (e) slant-stack gathers, and (f) angle gathers.

We note that all curves for the time-shift angle gathers have zero curvature at normal incidence. Therefore, the resolution of the time-shift mapping around normal incidence is lower than the corresponding space-shift resolution. However, the storage and computational cost of time-shift imaging is smaller than the cost of equivalent space-shift imaging. The choice of the appropriate imaging condition depends on the imaging objective and on the trade-off between the cost and the desired resolution.

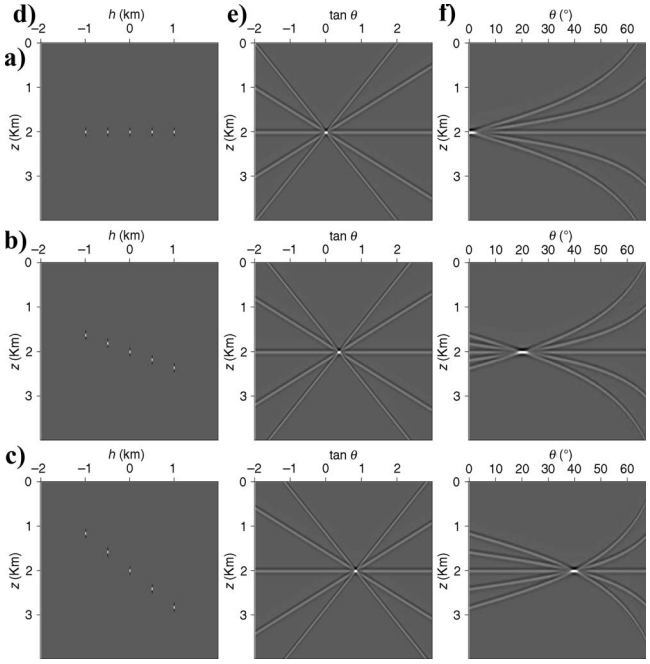


Figure 16. Image-gather formation using space-shift imaging. Horizontal rows depict events at (a) 0°, (b) 20°, and (c) 40°. Vertical columns correspond to subsampled, (d) space-shift gathers, (e) slant-stacked gathers, and (f) angle-gathers.

CONCLUSIONS

We develop a new imaging condition based on time shifts between source and receiver wavefields. This method is applicable to Kirchhoff, reverse-time, and wave-equation migrations and produces common-image gathers indicative of velocity errors. In wave-equation migration, time-shift imaging is more efficient than space-shift imaging because it only involves a simple phase shift prior to the application of the usual imaging crosscorrelation. Disk storage is also reduced, because the output volume depends on only one parameter (time shift $\boldsymbol{\tau}$) instead of three parameters (space shift $\mathbf{h}$). We show how this imaging condition can be used to construct angle gathers from time-shift gathers. More research is needed on how to utilize this new imaging condition for velocity and amplitude analysis.

ACKNOWLEDGMENT

We would like to acknowledge ExxonMobil for partial financial support of this research.

REFERENCES

Biondi, B., and P. Sava, 1999, Wave-equation migration velocity analysis: 69th Annual International Meeting, SEG, Expanded Abstracts, 1723–1726.

Biondi, B., and W. Symes, 2004, Angle-domain common-image gathers for migration velocity analysis by wavefield-continuation imaging: Geophysics, **69**, 1283–1298.

Claerbout, J. F., 1985, Imaging the earth's interior: Blackwell Scientific Publications, Inc.

Clapp, R. G., B. Biondi, and J. F. Claerbout, 2004, Incorporating geologic information into reflection tomography: Geophysics, **69**, 533–546.

de Bruin, C. G. M., C. P. A. Wapenaar, and A. J. Berkhout, 1990, Angle-dependent reflectivity by means of prestack migration: Geophysics, **55**,

1223–1234.
Faye, J. P., and J. P. Jeannot, 1986, Prestack migration velocities from focusing depth analysis: 56th Annual International Meeting, SEG, Expanded Abstracts, 438.
Fomel, S., 2004, Theory of 3-D angle gathers in wave-equation imaging: 74th Annual International Meeting, SEG, Expanded Abstracts, 1053.
MacKay, S., and R. Abma, 1992, Imaging and velocity estimation with depth-focusing analysis: Geophysics, **57**, 1608–1622.
———, 1993, Depth-focusing analysis using a wavefront-curvature criterion: Geophysics, **58**, 1148–1156.
Mosher, C., and D. Foster, 2000, Common angle imaging conditions for prestack depth migration: 70th Annual International Meeting, SEG, Expanded Abstracts, 830–833.
Nemeth, T., 1995, Velocity estimation using tomographic depth-focusing analysis: 65th Annual International Meeting, SEG, Expanded Abstracts, 465–468.
———, 1996, Relating depth-focusing analysis to migration velocity analysis: 66th Annual International Meeting, SEG, Expanded Abstracts, 463–466.
Paffenholz, J., B. McLain, J. Zaske, and P. Keliher, 2002, Subsalt multiple attenuation and imaging: Observations from the Sigsbee2B synthetic data set: 72nd Annual International Meeting, SEG, Expanded Abstracts, 2122–2125.
Prucha, M., B. Biondi, and W. Symes, 1999, Angle-domain common image gathers by wave-equation migration: 69th Annual International Meeting, SEG, Expanded Abstracts, 824–827.
Rickett, J. E., and P. C. Sava, 2002, Offset and angle-domain common image-point gathers for shot-profile migration: Geophysics, **67**, 883–889.
Sava, P., and B. Biondi, 2004a, Wave-equation migration velocity analysis, Part I: Theory: Geophysical Prospecting, **52**, 593–606.
———, 2004b, Wave-equation migration velocity analysis, Part II: Subsalt imaging examples: Geophysical Prospecting, **52**, 607–623.
———, 2005, Coordinate-independent angle-gathers for wave equation migration: 75th Annual International Meeting, SEG, Expanded Abstracts, 2052.
Sava, P. C., and S. Fomel, 2003, Angle-domain common-image gathers by wavefield continuation methods: Geophysics, **68**, 1065–1074.
Soubaras, R., 2003, Angle gathers for shot-record migration by local harmonic decomposition: 73rd Annual International Meeting, SEG, Expanded Abstracts, 889–892.
Stolk, C. C., and W. W. Symes, 2004, Kinematic artifacts in prestack depth migration: Geophysics, **69**, 562–575.
Xie, X., and R. Wu, 2002, Extracting angle domain information from migrated wavefield: 72nd Annual International Meeting, SEG, Expanded Abstracts, 1360–1363.